Synchrotron X-ray topography of electronic materials

T. Tuomi

Optoelectronics Laboratory, Helsinki University of Technology, PO Box 3000, FIN-02015 TKK, Finland.
E-mail: turkka.o.tuomi@hut.fi

Large-area transmission, transmission section, large-area back-reflection, back-reflection section and grazing-incidence topography are the geometries used when recording high-resolution X-ray diffraction images with synchrotron radiation from a bending magnet, a wiggler or an undulator of an electron or a positron storage ring. Defect contrast can be kinematical, dynamical or orientational even in the topographs recorded on the same film at the same time. In this review article limited to static topography experiments, examples of defect studies on electronic materials cover the range from voids and precipitates in almost perfect float-zone and Czochralski silicon, dislocations in gallium arsenide grown by the liquid-encapsulated Czochralski technique, the vapour-pressure controlled Czochralski technique and the vertical-gradient freeze technique, stacking faults and micropipes in silicon carbide to misfit dislocations in epitaxic heterostructures. It is shown how synchrotron X-ray topographs of epitaxic laterally overgrown gallium arsenide layer structures are successfully explained by orientational contrast.

Keywords: topography.

1. Introduction

X-ray diffraction topography using synchrotron radiation (Tuomi *et al.*, 1973, 1974) has developed during the past 30 years into a powerful materials characterization technique extremely well suited for defect studies of semiconductors and other electronic materials. Synchrotron X-ray topographs are diffraction images displaying defects and imperfections such as precipitates, voids, dislocations, stacking faults, strained layers and magnetic domain boundaries. The technique is rapid. Several high-resolution topographs are made on one film in an exposure time as short as 1 s. Topography measuring stations are available and used in all major synchrotron radiation facilities around the world. Fig. 1 shows a topography beamline at a synchrotron radiation facility (Rantamäki, 1999).

Both transmission geometry as illustrated in Fig. 1 and back-reflection geometry are being employed for the diffraction imaging of defects. Depending on the measuring geometry the synchrotron X-ray topographs are called large-area transmission, transmission section, large-area back-reflection, back-reflection section and grazing-incidence topographs (Rantamäki *et al.*, 2000). The distance from the source to the sample ranges from 30 m at the HASYLAB-DESY to 140 m at the ESRF. The longer the line and the smaller the source size, the better the image resolution that is achievable. The geometric resolution can be calculated from the equation

$$r = (s/L)w, \quad (1)$$

where s is the sample-to-film distance, L is the source-to-sample distance and w is the size of the source. The resolution r ranges from a few micrometres to values well below 1 μm. Kodak SO-343 X-ray films and Geola VRP-M holography films having a grain size of about 50 μm are commonly used and have been used for making the topographs presented in this review article. Instead of films, topographs are also frequently recorded on Ilford L4 25 μm or 50 μm nuclear emulsion plates. It is worth mentioning that, using synchrotron radiation, real-time diffraction imaging is possible because of the high intensity of the beam. The detector employed in this case is either a direct X-ray sensitive semiconductor charge-coupled device (CCD) (Tuomi *et al.*, 1992) or a fluorescent screen, which converts X-rays into visible light. The visible image is then magnified optically and viewed with a CCD camera. The spatial resolution is limited by the pixel size of the CCD element or by the grain size of the fluorescent screen.

Instead of a bending magnet (Fig. 1), a wiggler or an undulator without any optical element can also be employed as the source of synchrotron radiation. Mirrors, absorbing windows and monochromators are being used for beam conditioning to limit the spectral range and intensity. Care must be taken to avoid imaging the defects of the optical elements on top of those of the sample under investigation.

Image contrast depends on the geometry used and on the spectrum of the incident radiation. The contrast may be orientational, kinematical or dynamical even in the topographs recorded on the same film. In the case of bending-magnet radiation, the X-ray energies of the diffracted beam consist of a fundamental energy and some others related to the harmonics. The topographs are often simulated using models based on the kinematical or dynamical theory of X-ray diffraction.

2. Nearly perfect silicon

In extremely perfect and pure silicon grown by the float-zone technique, dynamical diffraction images of voids are observed in transmission topographs recorded at the undulator beamline BW1 at the Hamburger Synchrotrostrahlungslabor HASYLAB (Deslattes *et al.*, 1999; Tuomi *et al.*, 2001). The undulator spectrum was optimized for the third harmonic at 10.5 keV and further conditioned with a flat gold-coated silicon mirror. Fig. 2 shows typical images of voids, which are round spots having a black–white contrast and a diameter of 10–40 μm.

The black–white contrast follows the diffraction vector **g**. The reduction of the contrast on the positive side of the diffraction vector is explained by tensile strain of the lattice around voids close to the exit surface of the sample. The precipitates are seen as black–white dots too, but their contrast is opposite to that of the voids. Fig. 3 shows a 400 transmission topograph of a silicon sample cut from a crystal grown by the Czochralski technique. In this case, both voids and precipitates are imaged at the same time on the same film.

Precipitates are also seen in the section topographs of processed silicon wafers. Fig. 4 shows two transmission section topographs of Czochralski silicon (Rantamäki, 1999). For section topography the

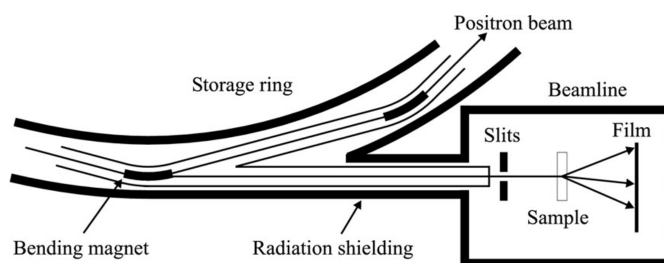

Figure 1
Topography beamline at a synchrotron radiation facility.

 © 2002 International Union of Crystallography • Printed in Great Britain – all rights reserved

beam in Fig. 1 is narrowed in the vertical direction by a slit having a width of about 15 μm. The interference fringes of the left-hand topograph are typical of a nearly perfect crystal, in which the defects are too small to be resolved using this imaging technique. The right-hand topograph is the cross-sectional image of an annealed wafer, where precipitates have grown to oxygen-induced stacking faults in the bulk. Only a very thin surface region is almost defect-free.

The depth of the denuded zone below the wafer surface, where there are no defects visible in the image, is easily measured from such topographs as shown in Fig. 4 (Rantamäki *et al.*, 1998). Strain gradient caused by process steps like oxidation shows up as increased X-ray intensity in the section topographs. The boundary between an epitaxic layer and the substrate is also seen as a dark line, *i.e.* as increased intensity of the diffracted beam, in similar topographs.

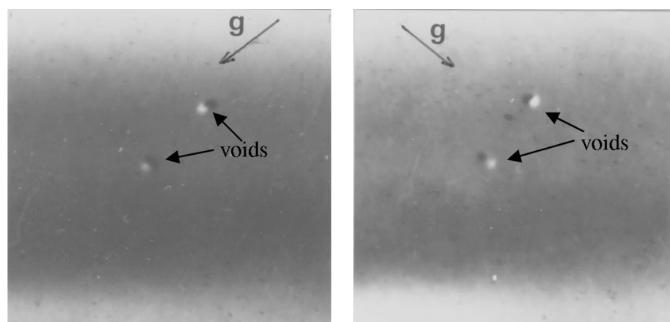

Figure 2
Stereo pair of synchrotron X-ray diffraction $1\bar{1}\bar{1}$ (left) and $\bar{1}1\bar{1}$ (right) topographs of float-zone silicon. The size of the square image is 1 mm × 1 mm.

Figure 3
A precipitate and several voids in the 400 transmission topograph of Czochralski silicon.

3. Gallium arsenide

Figs. 5, 6 and 7 show further examples of synchrotron X-ray transmission topographs of GaAs crystals. The crystals were grown by the liquid-encapsulated Czochralski technique (Prieur *et al.*, 1993), the vertical-gradient freeze technique (Prieur, 1997; Tuomi *et al.*, 1998) and the vapour-pressure-controlled Czochralski technique (Tuomi *et al.*, 2002), respectively. The series of images shows how the crystalline perfection of GaAs has improved from the typical cellular structure of dislocation networks in the early liquid-encapsulated Czochralski-grown material (Fig. 5) to crystals, in which large volumes are dislocation-free (Figs. 6 and 7).

The most prominent features of the GaAs topographs are the mostly curved black lines. They are images of dislocations. A particular dislocation line may not be visible with all Bragg reflections. The equation for disappearance is

$$\mathbf{g} \cdot \mathbf{b} = 0, \qquad (2)$$

where **b** is the Burgers vector of the dislocation.

If two topographs are found in which the dislocation is not visible, it is possible to determine the direction of **b**. Fig. 8 shows three topographs picked up from one film of a vertical-gradient freeze-grown GaAs sample. The dislocations marked with arrows in Fig. 8(*c*) are not visible in the two topographs of Figs. 8(*a*) and 8(*b*). When equation (2) is applied to these topographs, the result is **b** parallel to [011]. Most of the curved dislocations both in the vertical-gradient freeze-grown and in the vapour-pressure-controlled Czochralski GaAs crystals have a similar Burgers vector, *i.e.* **b** is along ⟨110⟩.

Examples from the literature show how the Burgers vector analysis of dislocations is successfully carried out from one set of transmission topographs containing several stereo pairs recorded on one film. It is worth noticing that the use of synchrotron radiation having a continuous spectrum of photon energies and a large intensity is the only practical way to obtain such a Laue pattern of transmission topographs from strongly absorbing materials like GaAs.

4. Silicon carbide

Dislocations in SiC wafers and diodes are analysed in the same way as dislocations in silicon and gallium arsenide (Prieur, 1997; Tuominen *et al.*, 2001; Yakimova *et al.*, 2002). Fig. 9 shows a back-reflection Laue pattern of topographs of a (0001) 4H-SiC wafer. A large number of usable topographs are recorded on the film.

Fig. 10 shows two back-reflection topographs selected from Fig. 9 of the silicon carbide wafer, on which diodes have been fabricated. The contours of the square diodes are seen in both topographs. In addition there are small circles, which are images of micropipes commonly observed in SiC grown by the modified Lely method. The

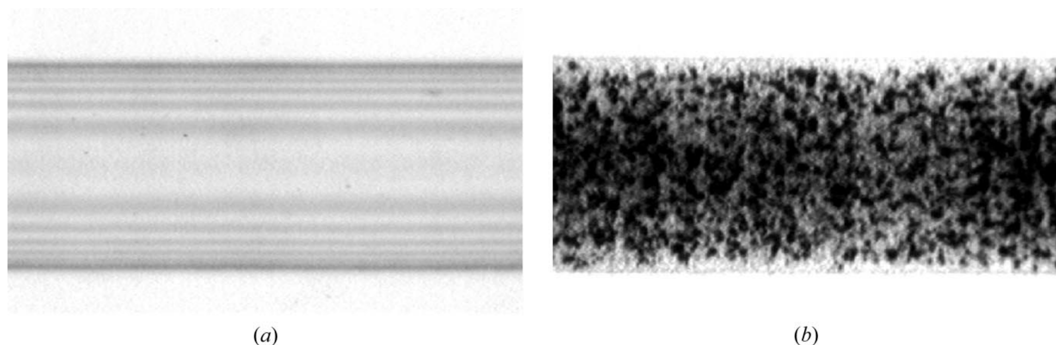

(*a*) (*b*)

Figure 4
Transmission section topographs of (*a*) as-grown and (*b*) annealed Czochralski silicon wafer.

diode fabrication has evidently produced triangular defects, which show up as dark areas in Fig. 10(*b*) and which are interpreted as images of stacking faults.

The topographs of Fig. 10 are important in helping to understand and improve crystal growth technology and device fabrication processes.

5. Epitaxic layer structures

Synchrotron X-ray topography has also been applied to structural studies of epitaxic layers (Hasenöhrl *et al.*, 2002; McNally, Danilewsky *et al.*, 1999; McNally, Tuomi *et al.*, 1999; McNally *et al.*, 2001; Rantamäki *et al.*, 1998; Rantamäki, Tuomi, Zytkiewicz, Dobosz & McNally, 1999; Rantamäki, Tuomi, Zytkiewicz, Domagala *et al.*, 1999). Fig. 11 shows a back-reflection topograph of an $In_{0.55}Ga_{0.45}P$ layer on a liquid-encapsulated Czochralski-grown GaAs substrate (Hasenöhrl *et al.*, 2002). A network of mutually perpendicular straight misfit dislocations is the dominant feature of the topograph. In addition, the cellular dislocation structure of the substrate is discernible on the background. This topograph is one from a series of similar topographs of $In_xGa_{1-x}P$–GaAs samples, for which topographs were used for the study of anisotropy and lattice relaxation.

Fig. 12 shows a back-reflection topograph of a $GaAs_{0.97}N_{0.03}$ layer grown by metal-organic vapour-phase epitaxy on a vertical-gradient freeze GaAs substrate. A misfit dislocation network has started to develop at the interface of a 140 nm-thick layer and the substrate. An X-ray diffraction curve shows that the layer is fully strained and relaxation is negligible. The synchrotron X-ray topography technique is, however, so sensitive that it reveals the minute relaxation of the lattice.

Fig. 13 shows an epitaxic GaAs layer structure grown on oxide stripes, which in turn have been deposited on a GaAs substrate (Rantamäki, Tuomi, Zytkiewicz, Dobosz & McNally, 1999; Rantamäki, Tuomi, Zytkiewicz, Domagala *et al.*, 1999). The epitaxic growth of GaAs begins at the seed windows opened by etching in the thin oxide mask covering the substrate. It then proceeds laterally over the oxide. After a while the homoepitaxial GaAs layer eventually merges into the adjacent laterally overgrown layer.

In the optical micrograph shown in Fig. 14(*a*) the epitaxic layers are white stripes. In Fig. 14(*b*) the topographic images of the layers are broad overlapping grey areas on both sides of the straight lines of the seed windows *w*. Fig. 14(*c*) shows the back-reflection section topograph made with a narrow beam having a width of about 15 µm. The images of the epitaxic layers are the wavy lines *e*–*e* crossing the substrate image *s*–*s* at the seed window *w* (see also Fig. 15).

The back-reflection section topographs evidently show images of bent epitaxic layers. Calculations based on a model of orientational contrast produce simulated images, which are in excellent agreement with the measured topographs seen in Fig. 15.

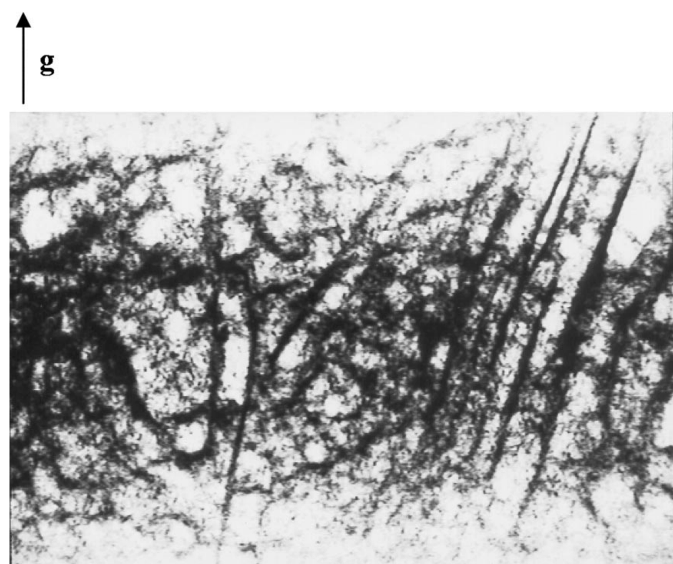

Figure 5
022 transmission topograph of liquid-encapsulated Czochralski-grown GaAs. The image size is 7 mm × 5 mm.

6. Summary

This review article is based on an invited lecture presented by the author at the Harima International Forum 2001. It describes the

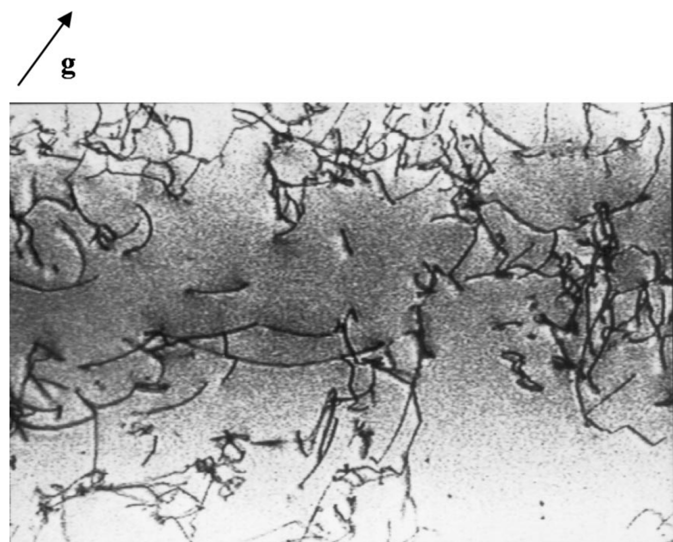

Figure 6
040 transmission topograph of vertical-gradient freeze-grown GaAs. The image size is 2 mm × 1 mm.

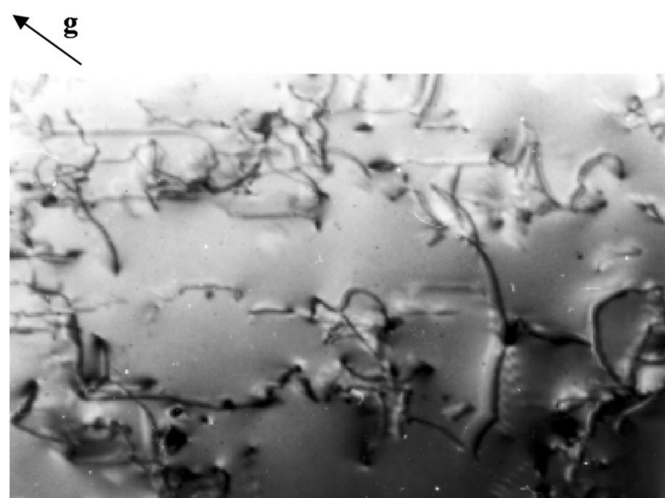

Figure 7
$\bar{1}31$ transmission topograph of vapour-pressure-controlled Czochralski-grown GaAs. The image size is 2 mm × 1 mm.

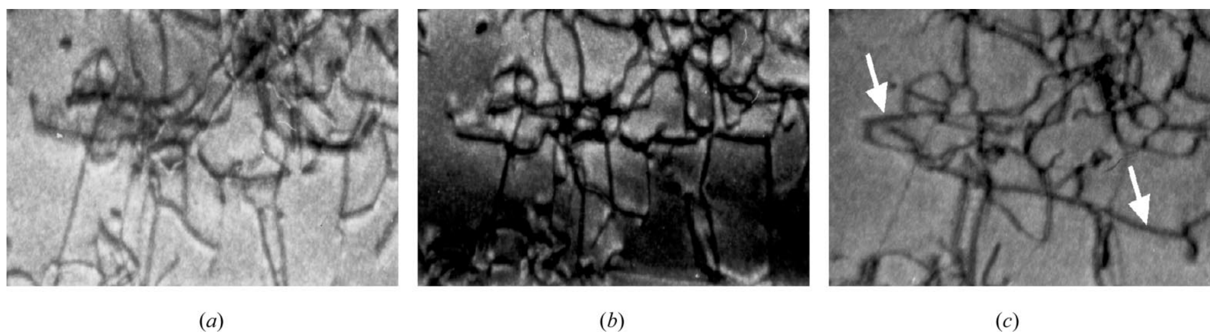
(a) (b) (c)

Figure 8
Transmission topographs of vertical-gradient freeze-grown GaAs: (*a*) $\bar{1}5\bar{5}$, (*b*) $\bar{1}\bar{5}5$ and (*c*) $\bar{1}55$ reflection.

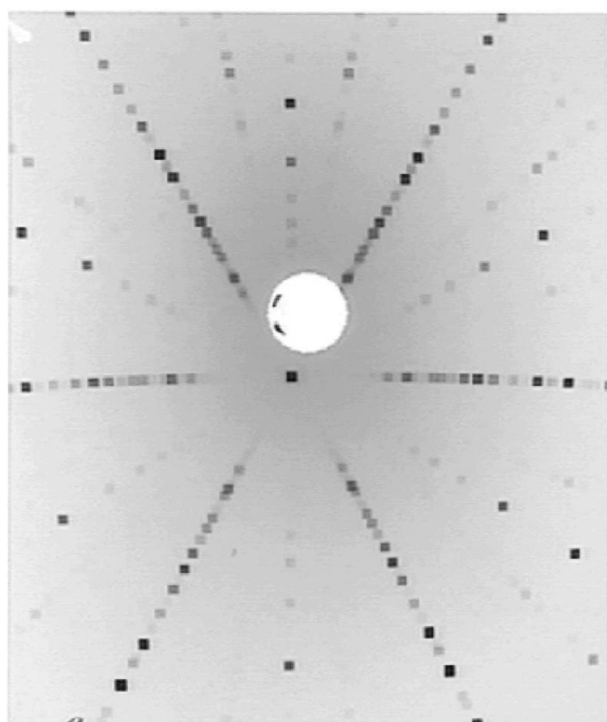

Figure 9
Back-reflection Laue pattern of topographs of 4H-SiC wafer. The film size is 100 mm × 120 mm.

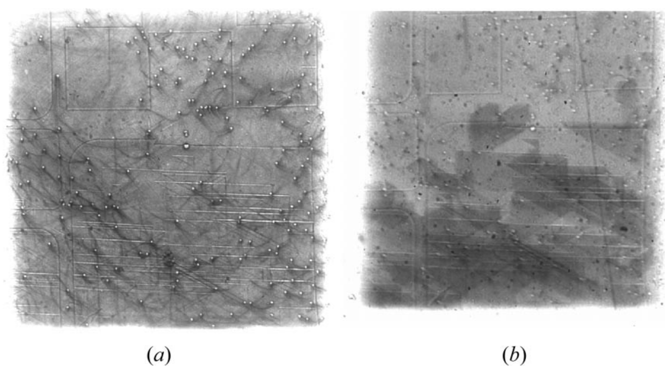
(a) (b)

Figure 10
Back-reflection topographs of SiC with square diodes. The image area is 1 mm × 1 mm.

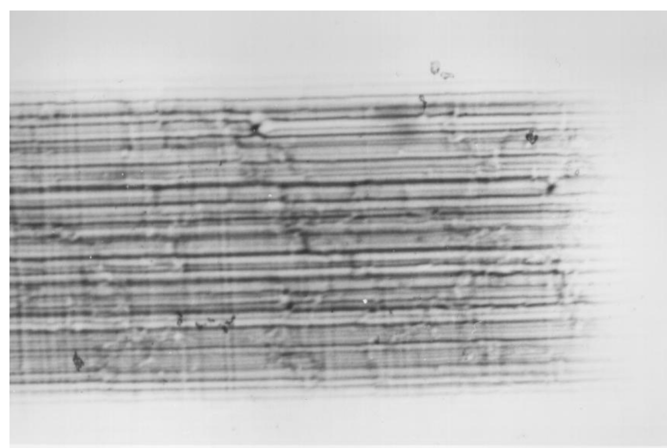

Figure 11
Back-reflection topograph of $In_{0.55}Ga_{0.45}P$ layer on GaAs. The image area is 1 mm × 2 mm.

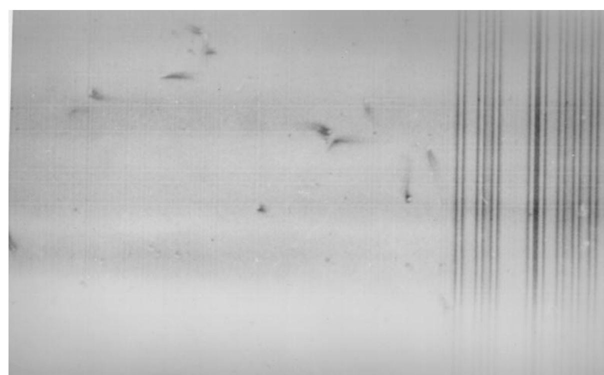

Figure 12
Back-reflection topograph of Ga $As_{0.97}N_{0.03}$ layer on GaAs. The image area is 1 mm × 2 mm.

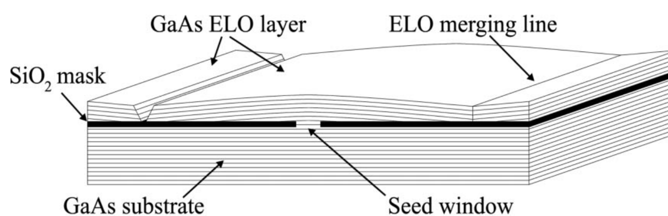

Figure 13
Epitaxically overgrown GaAs layers on GaAs substrate covered by SiO_2 mask.

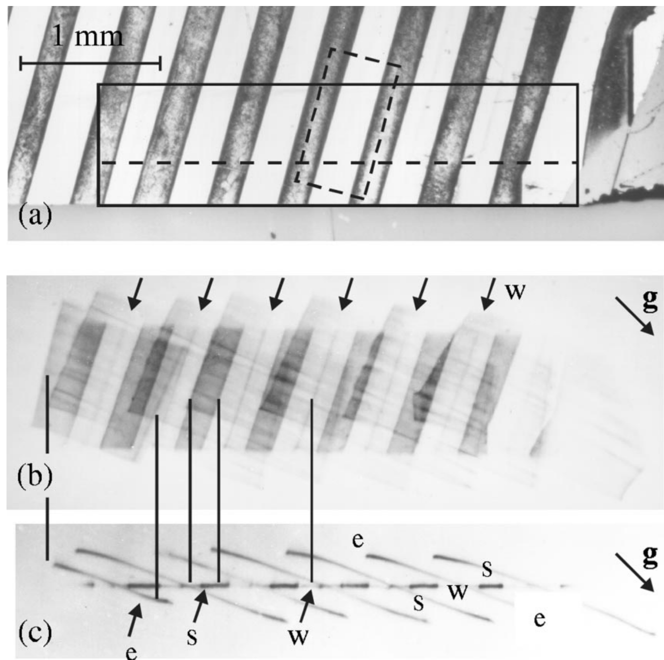

Figure 14
(*a*) Optical micrograph, (*b*) back-reflection and (*c*) back-reflection section topograph of epitaxically laterally overgrown GaAs sample. *e* is the epitaxic layer, *s* is the substrate and *w* is the window.

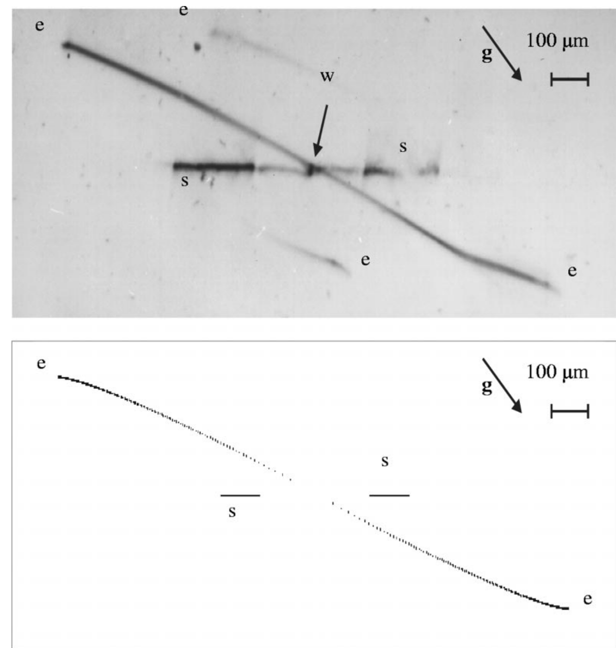

Figure 15
Measured and calculated back-reflection section topograph of epitaxically laterally overgrown GaAs sample. *e–e* is the epitaxic layer, *s–s* is the substrate and *w* is the window. Bragg reflection is 026.

imaging technique called X-ray diffraction topography using synchrotron radiation. Transmission and back-reflection geometries are illustrated. In a number of cases more than one geometry and a special beam conditioning are needed to obtain a concise picture of defects in an electronic material. The works presented in this article are exclusively on semiconductor single crystals and heterostructures, although the imaging technique has been applied to other materials too. These include magnetic and ferroelectric as well as materials for optical waveguides.

High-resolution diffraction images of defects in electronic materials are obtained in short exposure times using synchrotron radiation. Voids and precipitates are observed in perfect float-zone and Czochralski silicon. Their defect contrast is dynamical and observed only with low-energy photons. The Burgers vector of a dislocation in a semiconductor is determined from the topographs of one Laue pattern recorded on one high-resolution film at a very short exposure time. Topographs of epitaxic laterally overgrown electronic materials are explained by orientational contrast of bent layers.

Contributions by E. Prieur, R. Rantamäki, J. Partanen, M. Tuominen, A. Ellison, M. Karilahti, L. Knuuttila, J. Riikonen, J. Toivonen, P. J. McNally, D. Lowney, W. Chen, J. Kanatharana, M. O'Hare, A. N. Danilewsky, Z. R. Zytkiewicz, P. Bergman, H. Jacobson, P. Becker, S. Hasenöhrl and P. Rudolph are gratefully acknowledged. The author is also grateful to T. Wroblewski, D. Novikov and G. Materlik at the beamlines F1 and BW1 at the HASYLAB-DESY, and J. Härtwig and J. Baruchel at the beamline ID19 at the ESRF.

References

Deslattes, R. D., Kessler, E. G. Jr, Owens, S., Black, D. & Henins, A. (1999). *J. Phys. D*, **32**, A3–A7.
Hasenöhrl, S., Kudela, R., Novak, J., Tuomi, T. O. & Knuuttila, L. (2002). *Mater. Sci. Eng. B*, **88**, 134–138.
McNally, P. J., Danilewsky, A. N., Curley, J. W., Reader, A., Rantamäki, R., Tuomi, T., Bolt M. & Taskinen, M. (1999). *Microelectron. Eng.* **45**, 47–56.
McNally, P. J., Tuomi, T., Lowney, D., Jacobs, K., Danilewsky, A. N., Rantamäki, R., O'Hare, M. & Considine, L. (2001). *Phys. Status Solidi A*, **185**, 373–382.
McNally, P. J., Tuomi, T., Rantamäki, R., Jacobs, K., Considine, L., O'Hare, M., Lowney, D. & Danilewsky, A. N. (1999). *Mater. Res. Soc. Symp. Proc.* **572**, 327–332.
Prieur, E. (1997). DSc (Tech.) thesis, Helsinki University of Technology, Finland.
Prieur, E., Tuomi, T., Partanen, J., Yli-Juuti, E. & Tilli, M. (1993). *J. Cryst. Growth*, **132**, 599–605.
Rantamäki, R. (1999). DSc (Tech.) thesis, Helsinki University of Technology, Finland.
Rantamäki, R., Tuomi, T., McNally, P. J., Curley, J. & Danilewsky, A. (1998). *J. X-ray Sci. Technol.* **8**, 159–169.
Rantamäki, R., Tuomi, T., Zytkiewicz, Z. R., Dobosz, D. & McNally, P. J. (1999). *J. Phys. D*, **32**, A114–A118.
Rantamäki, R., Tuomi, T., Zytkiewicz, Z. R., Domagala, J., McNally, P. J. & Danilewsky, A. N. (1999). *J. Appl. Phys.* **86**, 4298–4303.
Rantamäki, R., Tuomi, T., Zytkiewicz, Z. R., McNally, P. J. & Danilewsky, A. N. (2000). *J. X-ray Sci. Technol.* **8**, 277–288.
Tuomi, T., Juvonen, M., Rantamäki, R., Hjelt, K., Bavdaz, M., Nenonen, S., Gagliardi, M.-A., McNally, P. J., Danilewsky, A. N., Prieur, E., Taskinen, M. & Tuominen, M. (1998). *Mater. Res. Soc. Symp. Proc.* **487**, 459–464.
Tuomi, T., Knuuttila, L., Riikonen, J., McNally, P. J., Chen, W., Kanatharana, J., Neubert, M. & Rudolph, P. (2002). *J. Cryst. Growth*. In the press.
Tuomi, T., Naukkarinen, K., Laurila, E. & Rabe, P. (1973). *Acta Polytech. Scan. Phys. Incl. Nucleon. Ser.* **100**, 1–8.
Tuomi, T., Naukkarinen, K. & Rabe, P. (1974). *Phys. Status Solidi A*, **25**, 93–106.
Tuomi, T., Partanen, J. & Simomaa, K. (1992). *Rev. Sci. Instrum.* **63**, 682–684.
Tuomi, T., Rantamäki, R., McNally, P. J., Lowney, D., Danilewsky, A. N. & Becker, P. (2001). *J. Phys. D*, **34**, A133–A135.
Tuominen, M., Ellison, A., Tuomi, T., Yakimova, R., Milita, S. & Janzén, E. (2001). *J. Cryst. Growth*, **225**, 23–33.
Yakimova, R., Syväjärvi, M., Jacobsson, H., Kakanakova-Georgieva, A., Tuomi, T., Rendakova, S., Dmitriev, V. & Janzén, E. (2002). *Mater. Res. Soc. Symp. Proc.* In the press.

 Received 8 December 2001 • Accepted 5 March 2002